ARTICLES
https://doi.org/10.1038/s41563-019-0445-x
nature materials

Bio-inspired hydrophobicity promotes CO_2 reduction on a Cu surface

David Wakerley[1], Sarah Lamaison[1], François Ozanam[2], Nicolas Menguy[3], Dimitri Mercier[4], Philippe Marcus[4], Marc Fontecave[1*] and Victor Mougel[1,5*]

The aqueous electrocatalytic reduction of CO_2 into alcohol and hydrocarbon fuels presents a sustainable route towards energy-rich chemical feedstocks. Cu is the only material able to catalyse the substantial formation of multicarbon products (C_2/C_3), but competing proton reduction to hydrogen is an ever-present drain on selectivity. Here, a superhydrophobic surface was generated by 1-octadecanethiol treatment of hierarchically structured Cu dendrites, inspired by the structure of gas-trapping cuticles on subaquatic spiders. The hydrophobic electrode attained a 56% Faradaic efficiency for ethylene and 17% for ethanol production at neutral pH, compared to 9% and 4% on a hydrophilic, wettable equivalent. These observations are assigned to trapped gases at the hydrophobic Cu surface, which increase the concentration of CO_2 at the electrode–solution interface and consequently increase CO_2 reduction selectivity. Hydrophobicity is thus proposed as a governing factor in CO_2 reduction selectivity and can help explain trends seen on previously reported electrocatalysts.

Figure 1a shows a theorized sustainable energy cycle propagated through the storage of renewable energies as CO_2-derived fuel. Such a process would provide relief to numerous environmental concerns, both current and impending[1], and curtail dependency on fossil fuel. The cycle is driven through aqueous CO_2 electrolysis, wherein electrons and protons from water oxidation are used in the reduction of CO_2 to hydrocarbons and alcohols. Contemporary research now seeks an efficient and inexpensive catalyst for this reduction.

Cu remains the paradigmatic surface for CO_2 reduction, with the ability to produce C_2 and C_3 species, such as ethylene, ethanol and *n*-propanol[2]. The formation of such products has various thermodynamic and kinetic demands and requires multiple proton and electron transfers (Fig. 1b). These are readily facilitated in water, but proton reduction to H_2 is more facile than CO_2 reduction (red square in Fig. 1b)[3]. Water is also in substantial excess due to the low solubility of CO_2 (33 mM at room temperature)[4]; as a result, Cu electrodes typically lose >30% of their Faradaic efficiency (FE) to H_2 production[5].

The fabrication of electrodes with high selectivity towards CO_2 reduction, particularly towards products that contain multiple carbons, remains a major priority in this field. Hitherto implemented strategies include surface modifications[6,7], adjusting surface pH[8] and the use of non-aqueous solvents[9]; however, the most effective approaches can be summarized into three categories: (1) Morphology: nanowires[10], nanowhiskers[11], nanoparticles[12], nanoprisms[13] and nanodendrites[14,15] present high catalytic surface areas that show appreciable selectivity. (2) Carbon supports: carbon frameworks and gas-diffusion layers loaded with Cu show the generation of C_2 products with up to 80% FE[16–19]. (3) Oxide layers: surface oxides serve as precursors to active Cu catalysts, which present FEs as high as 60% for ethylene formation[20–22].

These strategies may also increase the hydrophobicity of an electrode, but this is rarely discussed as a determinant on selectivity[2]. Submerged hydrophobic surfaces trap appreciable amounts of gas at the nanoscale[23,24], and even at the microscale if the Cassie–Baxter regime is reached[25], which would allow gaseous CO_2 to accumulate at the Cu–solution interface. Recent reports have exploited gas–electrode–solution triple-phase boundaries to increase the CO_2 reduction activity of Cu on gas-diffusion electrodes with hydrophobic polytetrafluoroethylene layers[18,19]; however, it is difficult to assign this enhancement solely to hydrophobicity over other factors, such as their porosity and increased mass transport of CO_2[26]. Here, we thus study hydrophobicity as an isolated parameter on a Cu surface to establish its role in promoting gas trapping and consequently selective CO_2 reduction.

Taking nature as inspiration, we introduce hydrophobicity based on the 'plastron effect' used by aquatic arachnids, such as the diving bell spider (Fig. 1c)[27]. These plastrons are composed of hydrophobic hairs that trap air and thereby allow the spider to respire under water. The gas-trapping phenomenon occurs when hydrophobicity is simultaneously presented on microscale and nanoscale surface structuration[28]. We achieved an analogous multiscale hydrophobic surface through modification of hierarchically structured dendritic Cu with a monolayer of waxy alkanethiol. The resultant electrode visibly trapped CO_2 gas at the electrolyte–electrode interface to form a triple-phase boundary (Fig. 1d). As a result, H_2 evolution on this surface was substantially lowered in CO_2-saturated electrolyte compared to an unmodified hydrophilic equivalent, from 71% FE to 10%, whereas CO_2 reduction increased from 24% to 86%, of which C_2 products comprised 74% FE. The drastically increased CO_2 concentration at the hydrophobic Cu surface was identified as key to the increased catalytic selectivity, which we propose is present in other reported systems.

[1]Laboratoire de Chimie des Processus Biologiques, CNRS UMR 8229, Collège de France, Paris, France. [2]Laboratoire de Physique de la Matière Condensée, CNRS-École Polytechnique, Palaiseau Cédex, France. [3]Sorbonne Université, UMR CNRS 7590, MNHN, IRD, Institut de Minéralogie, de Physique des Matériaux et de Cosmochimie, IMPMC, Paris, France. [4]Physical Chemistry of Surfaces Group, ChimieParisTech-CNRS, Institut de Recherche de Chimie Paris, Paris, France. [5]Present address: Department of Chemistry and Applied Biosciences, Laboratory of Inorganic Chemistry, Swiss Federal Institute of Technology Zürich, Zürich, Switzerland. *e-mail: marc.fontecave@college-de-france.fr; mougel@inorg.chem.ethz.ch

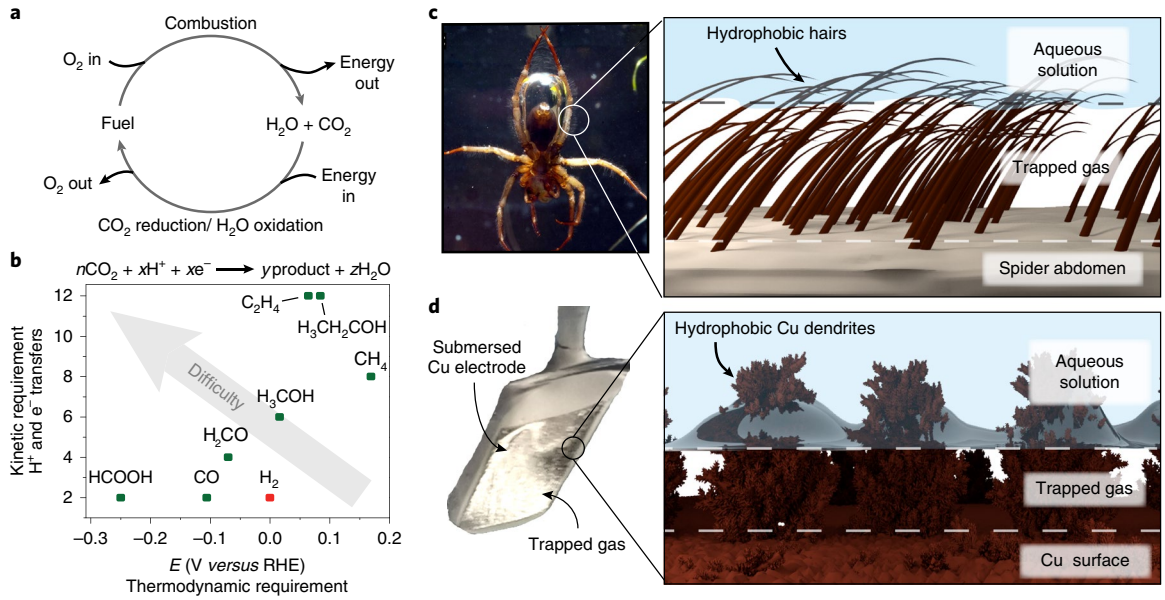

Fig. 1 | CO_2 reduction as a source of sustainable fuel and an introduction to the plastron effect. a, The generation of renewable fuel through CO_2 reduction and H_2O oxidation. **b**, The kinetic versus thermodynamic requirement of various CO_2 reduction reactions[3]. The plotted values are based on the reaction equation given above the graph, made stoichiometric according to the product composition. **c**,**d**, The plastron effect: the use of a hydrophobic surface to trap a layer of gas between the solution–solid interface. This is illustrated on a diving bell spider for subaquatic breathing in **c** and on a hydrophobic dendritic Cu surface for aqueous CO_2 reduction in **d**. The photo of the diving bell spider is adapted from Seymour and Hetz[42] with permission from The Company of Biologists.

Hydrophobic Cu dendrite preparation and characterization

Cu dendrite scaffolds were grown using previously reported aqueous electrodeposition procedures, which produced hierarchical architectures with both micro- and nanoscale features (Supplementary Fig. 1)[29,30]. Powder X-ray diffraction measurements confirmed the structure to be metallic Cu (Fig. 2a), although a small amount of Cu_2O was visible (Supplementary Fig. 2). The hydrophobic treatment was undertaken by submersing the dendritic Cu into liquid 1-octadecanethiol at 60 °C for 15 minutes to form an alkanethiol layer. Transmission electron microscopy (TEM) of the dendritic Cu after treatment confirmed that the nanostructure remained intact (Fig. 2b) and was coated with a monolayer between 2 and 3 nm in thickness (Fig. 2c), consistent with a surface of 1-octadecanethiol molecules bound upright (the chain length is 2.3 nm between the surface-bound S and terminal C). The carbonaceous nature of the coating was confirmed by energy-filtered transmission electron microscopy (EF-TEM) at the C-K edge (white regions in Fig. 2d). X-ray energy-dispersive spectroscopy of the area indicated in Fig. 2d (yellow circle) displayed S and C environments within the layer (Supplementary Fig. 3) and no carbonaceous layer was present on untreated Cu dendrite (Supplementary Fig. 4).

The alkanethiolation removes Cu oxide from the surface to leave Cu–S bonds, as illustrated by X-ray photoelectron spectroscopy (XPS) (Fig. 2e)[31]. Before treatment, the Cu dendrite shows environments consistent with Cu^{I}_2O at 932.5/952.4 eV and $Cu^{II}O$ at 934.6/955.0 eV and 942.8/962.7 eV. Analysis of the Cu LMM Auger showed no evidence of metallic Cu^0 at the surface (Supplementary Fig. 5)[32]. After reaction with 1-octadecanethiol, all the Cu^{II} environments were removed to form a surface of Cu^{I} (Fig. 2e and Supplementary Table 1), and a new S 2*p* peak is visible at 163.0 eV, consistent with Cu–S bonds (Fig. 2f)[32]. The presence of the alkanethiol layer was further confirmed through attenuated total reflectance-Fourier transform infrared (ATR-FTIR) spectroscopy (Supplementary Fig. 6).

Contact angle measurements illustrated that without the 1-octadecanethiol modification, the Cu dendrite surface is hydrophilic; a deposited water droplet sat with a contact angle of 17° (Fig. 2g). The alkanethiol-treated electrode is not susceptible to the same wetting, with a drastically increased contact angle of 153° (Fig. 2h). This falls into the regime of superhydrophobicity in which trapped gases are expected on both the micro- and nanoscale[33]. For clarity, these electrodes are referred to as the wettable dendrite and hydrophobic dendrite for the hydrophilic and hydrophobic dendritic Cu surfaces, respectively.

The initial characterization of the dendrites' electrochemical properties revealed a significant decrease in electrochemically active surface area (ECSA) on the introduction of hydrophobicity. Capacitance measurements of the hydrophobic dendrite indicated the surface had very limited electrical contact with the solution as it displayed an ECSA of 3×10^{-3} $cm^2\,cm^{-2}$, much lower than the 21 $cm^2\,cm^{-2}$ obtained on the wettable dendrite (where $cm^2\,cm^{-2}$ indicates the ECSA of the dendritic electrode versus that of a flat Cu electrode) (Supplementary Fig. 7). Brunauer–Emmett–Teller (BET) analysis through Kr-adsorption measurements revealed that the ECSA disparity is not from a loss in geometric surface area on alkanethiol treatment, as these remained similar: 90 $cm^2\,cm^{-2}$ and 92 $cm^2\,cm^{-2}$ for the wettable dendrite and hydrophobic dendrite, respectively (where $cm^2\,cm^{-2}$ indicates the BET-derived surface area of the dendritic electrode versus the area of a flat electrode). The decrease in ECSA is therefore induced by gas trapping at the interface between the hydrophobic dendrite and the solution, as illustrated in Fig. 2j (top).

On the application of a reducing potential over 60 minutes in an aqueous electrolyte (0.1 M $CsHCO_3$, CO_2 saturated) the ECSA of the hydrophobic dendrite increased to 0.2 $cm^2\,cm^{-2}$ (Supplementary Fig. 7c), which can also be seen through linear sweep voltammetry (LSV) (Supplementary Fig. 8). This increase is assigned to the loss of 1% of alkanethiol when labile Cu^0 oxidation states are reached, as the ECSA is 1% of the wettable dendrite (21 $cm^2\,cm^{-2}$). This

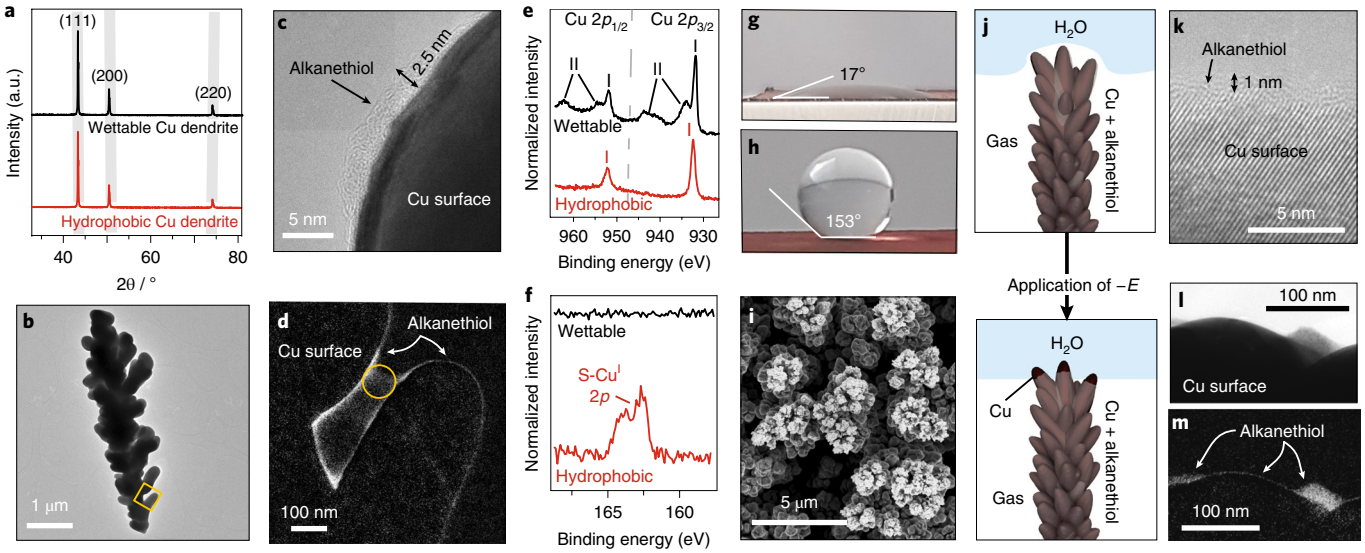

Fig. 2 | Characterization of the electrode surface. a, Powder X-ray diffraction of the Cu dendrite with and without hydrophobic surface treatment. **b**,**c**, The TEM (**b**) and high-resolution TEM (**c**) images of a 1-octadecanethiol-treated Cu dendrite show the layer of alkanethiol attached to the Cu surface; the yellow square in **b** indicates the area observed in **d**. **d**, EF-TEM using the C-K edge of an alkanethiol-treated Cu dendrite surface; the yellow circle indicates the area used for the TEM–X-ray energy-dispersive spectroscopy analysis in Supplementary Fig. 3. **e**, The XPS spectra in the Cu regions show peaks assigned to the I and II oxidation states. **f**, The XPS spectra show the presence of S on the alkanethiol-treated Cu surface. **g**,**h**, The contact angle measurements of the wettable (**g**) and hydrophobic (**h**) dendrite. **i**, SEM image of the hydrophobic dendrite after 2.5 h of an applied cathodic potential in 0.1 M $CsHCO_3$ (CO_2 saturated, pH 6.8, room temperature) with a CO_2 flow of 10 ml min^{-1}. **j**, Illustration of the hydrophobic dendrite gaining a solid–liquid interface on the application of a negative potential. **k**–**m**, Equivalent images from **c** (**k**) and **d** (**l** and **m**) after electrolysis in 0.1 M $CsHCO_3$ (CO_2 saturated, pH 6.8, room temperature) with a CO_2 flow of 10 ml min^{-1} for 30 min at –1.4 V versus RHE.

loss occurs at the point of the electrode closest to the electrolyte, as suggested through scanning electron microscopy (SEM) images that show brighter Cu regions at the tips of the dendrite (Fig. 2i and Supplementary Fig. 9). Similar activation is documented on other hydrophobic electrodes[25]. The hydrophobic dendrite therefore requires an initial application of potential to generate a stable liquid–electrode–gas triple-phase boundary at the top of the dendrite where electrochemical reactions take place, as illustrated in Fig. 2j. This activation was monitored through one day of repeated LSV scans, wherein the current at –1.4 V versus the reversible hydrogen electrode (RHE) stabilized 3–5 times lower than that of the wettable equivalent (Supplementary Fig. 10).

To ensure the hydrophobic dendrite maintained its hydrophobicity on the application of a negative potential, contact angle measurements were carried out after 12 hours of electrolysis at –15 mA cm^{-2} (Supplementary Fig. 11). The resultant angle of 143° indicated that the hydrophobic surface treatment was not removed. Furthermore, ^{1}H-NMR spectroscopy showed no 1-octadecanethiol within the electrolyte after electrolysis (Supplementary Fig. 12), although some dissolved alkanethiol may have been present below the detection limit of the experiment. XPS analysis before and after the electrolysis showed similar ratios of Cu:S on the sample (Supplementary Table 2); however, a portion of the 1-octadecanethiol was converted into alkanesulfonates (168.6 eV peak in Supplementary Fig. 5c), which is known to occur on the exposure of alkanethiol monolayers to air[34]. Nevertheless, high-resolution TEM and EF-TEM at the C-K edge (Fig. 2k–m) do show that the monolayer loses density and that large carbonaceous deposits are present on the nanostructure after electrolysis. We thus propose that the majority of the C_{18}-alkane chain does not dissolve from the electrode surface, but a portion may move across the surface to form aliphatic agglomerates, which explains how the surface maintains hydrophobicity while cathodic current passes.

Catalytic activity of hydrophobic and wettable Cu dendrites

Figure 3a shows the LSV of the hydrophobic dendrite and equivalent wettable dendrite in a CO_2-saturated $CsHCO_3$ electrolyte (0.1 M, pH 6.8). Cs^+ cations were used due to their superior ability to buffer pH changes at the electrode–solution interface during electrolysis compared to other cations[35], which thereby eliminated changes in surface pH as a determinant on selectivity. To reach a current of –5 mA cm^{-2}, the wettable dendrite required a potential of –0.68 V versus RHE, whereas the hydrophobic dendrite required a more negative potential of –1.38 V versus RHE. The lowered current at a given potential can be partly explained by the significantly lower ECSA of the hydrophobic dendrite, but should also be assigned to the lack of proton reduction activity exhibited by this electrode. Controlled potential electrolysis (CPE) confirmed this, as even at highly cathodic potentials the hydrophobic dendrite had a vastly lowered H_2 evolution activity: at –1.6 V versus RHE, the hydrophobic dendrite displayed a H_2 evolution FE below 10%, whereas the wettable one displayed values above 60% (Fig. 3b,c). In place of the H_2 evolution, the hydrophobic dendrite presented a superior CO_2 reduction efficiency for both C_1 and C_2 products (Fig. 3b,c), except at –1.2 V versus RHE, at which point the current was too low to detect C_2 products (Supplementary Fig. 13). To confirm that the optimal CO_2 reduction selectivity on the wettable dendrite was not attained at lower potentials, CPE at less cathodic biases was carried out (Supplementary Fig. 14).

During electrolysis, CO_2 was introduced as a stream of gas from the bottom of the cell (Supplementary Fig. 15). With the hydrophobic dendrite, the capture and retention of the gaseous CO_2 stream was observed, which caused a bubble to engulf the entire electrode surface (Fig. 3e and Supplementary Video 1). If the gas flow was not incident to the hydrophobic dendrite to constantly refill this bubble, the formation of C_1 and C_2 products was severely reduced (Fig. 3d), which indicates that the captured CO_2 at the electrode surface was

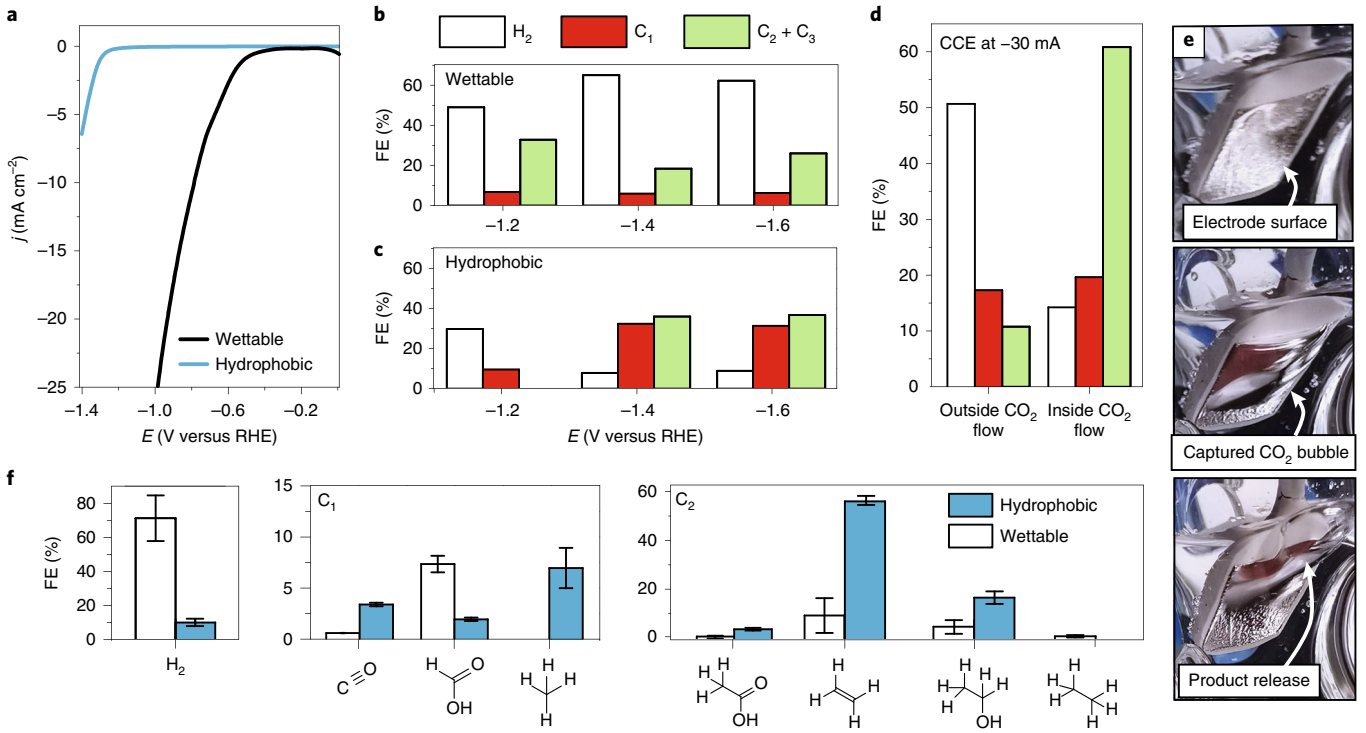

Fig. 3 | The effect of hydrophobicity on electrocatalytic CO_2 reduction. a, LSV of the wettable and hydrophobic dendrite ($\nu = 20$ mV s^{-1}). **b**,**c**, CPE product FEs from the wettable (**b**) and hydrophobic (**c**) dendrite at various potentials. **d**, Product formation FE at the hydrophobic dendrite after CCE at −30 mA cm^{-2} inside and outside the CO_2 flow at 2.5 ml min^{-1}. **e**, Photos of the capture and release of a CO_2 bubble on the hydrophobic dendrite surface. **f**, Product formation FEs at the hydrophobic versus wettable dendrite when passing an overall current density of −30 mA cm^{-2}. Gaseous products were analysed after 10 and 30 min and liquid products after 35 min of electrolysis. In all cases, the electrolyte was CO_2-saturated $CsHCO_3$ (0.1 M, pH 6.8, room temperature). Unless stated otherwise, a CO_2 flow rate of 5 ml min^{-1} was used throughout the electrolysis. Error bars are based on the s.d. of three individual measurements.

the predominant substrate of the hydrophobic dendrite. At lower partial pressures of CO_2 in the gas stream the CO_2 reduction rate dropped accordingly (Supplementary Fig. 16).

Control experiments without a hierarchical Cu surface morphology were undertaken using a flat Cu electrode treated with 1-octadecanethiol. Neither gas trapping nor large contact angles were observed (contact angle of 90°) (Supplementary Fig. 17) and the electrode did not show a drastic increase in selectivity for CO_2 reduction compared to a pristine Cu electrode (Supplementary Table 3). The combination of hydrophobic treatment and hierarchical morphology therefore facilitates gas trapping.

Controlled current electrolysis (CCE) at −30 mA cm^{-2} for the two Cu dendrites was undertaken to understand their selectivity while exerting the same mass transport pressure on the solution (Fig. 3f). The hydrophobic dendrite required a higher cathodic applied potential to reach −30 mA cm^{-2} ($E = -1.1$ to −1.5 V versus RHE, ohmic-drop corrected), but had much higher FEs for CO_2 reduction: CO (3% hydrophobic, 1% wettable), methane (7% hydrophobic, 0% wettable), ethylene (56% hydrophobic, 9% wettable), ethanol (17% hydrophobic, 4% wettable) and acetic acid (1% hydrophobic, 0.4% wettable). In contrast, the wettable dendrite required a less cathodic potential to reach −30 mA cm^{-2} ($E = -0.8$ to −1.0 V versus RHE, ohmic-drop corrected) as it carried out mostly H_2 evolution (10% hydrophobic, 71% wettable); however, it also showed the highest selectivity for formate (2% hydrophobic, 7% wettable), ethane (0% hydrophobic, 0.5% wettable) and *n*-propanol formation (0% hydrophobic, 2% wettable, not pictured). The hydrophobic dendrite's selectivity for C_2 products (74% total) rivals that of state-of-the-art gas-diffusion electrode systems in alkaline conditions (66% ethylene, 11% ethanol and 6% acetate)[19]; however, the achieved currents and required overpotentials are poorer in the neutral pH electrolyte.

Extended CO_2 reduction on the hydrophobic dendrite over five hours at a controlled current density of −30 mA cm^{-2} showed high ethylene and ethanol FEs of 30–55% and 12–22%, respectively (Supplementary Fig. 18). During the experiment, C_2-product formation was again sensitive to interaction with inbound CO_2: drops in C_2 production were observed when the CO_2 flow fell out of line with the electrode surface (Supplementary Fig. 18, as indicated), but the stream could be adjusted to restore activity. Despite this, a gradual decrease in C_2-production activity was apparent, coincident with the destruction of regions of the dendrite surface (Supplementary Fig. 19). This destruction was assigned to the mechanical stress imposed by the continual collision of bubbles with the electrode surface. Engineering efforts using vapour-fed electrodes to relieve this stress are ongoing.

The gas trapping of the hydrophobic dendrite could also be exploited for CO reduction, for which the low substrate concentration is particularly problematic ([CO] = 1 mM at 1 atm at room temperature)[4]. The CCE at −30 mA cm^{-2} in a CO flow on the hydrophobic dendrite showed a 23.5% FE for CO reduction, compared to 0.88% on the wettable dendrite in 1 M KOH (Supplementary Fig. 20 and Supplementary Table 4). Further experiments showed that the C_2 selectivity during CO reduction on the hydrophobic dendrite was greatly promoted in pH 14 solution (1 M KOH C_1:C_2 ratio = 1:24), in comparison to pH 7 (0.1 M potassium phosphate buffer (KPi) C_1:C_2 ratio = 1:1.7) (Supplementary Fig. 20). Additional CO_2 reduction experiments in more acidic conditions (pH 4.6, CO_2-saturated 0.1 M KPi) similarly showed a decrease in C_2 selectivity (C_1:C_2

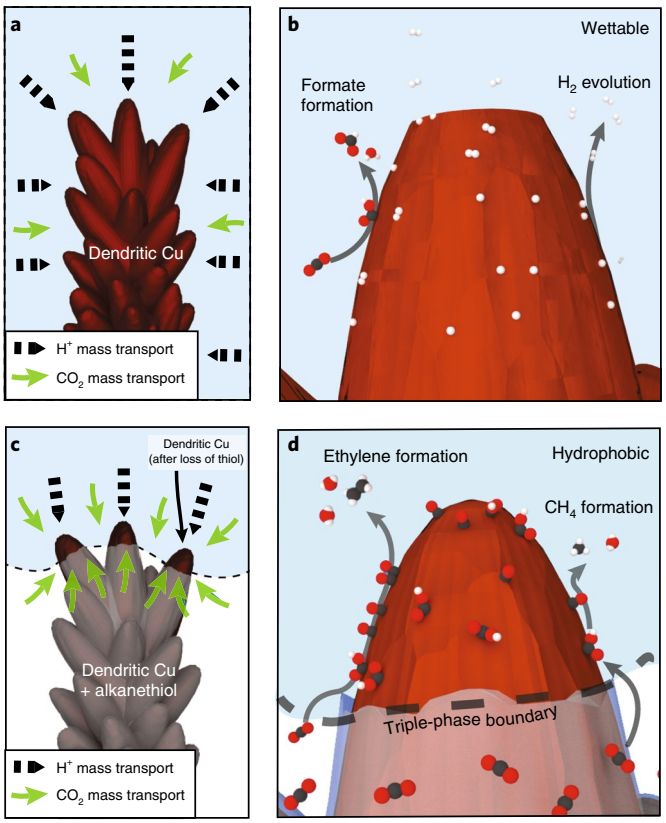

Fig. 4 | The proposed role of hydrophobicity in promoting CO_2 reduction over proton reduction. a,**b**, The illustrations of the wettable dendrite under operation show the reactant mass transport and product formation on the electrode surface. **c**,**d**, The illustrations of the operation of the hydrophobic dendrite show the enhanced CO_2 mass transport from the triple-phase boundary between the electrolyte, electrode and gaseous CO_2 and the resultant formation of key products on the surface.

ratio = 1:0.8) (Supplementary Fig. 21 and Supplementary Table 5). Formic acid reduction experiments produced only H_2, which excludes it as a source of C_2 products (Supplementary Table 6).

An explanation of the reported data is given in Fig. 4, which shows a single strand of the dendritic Cu in its wettable (Fig. 4a,b) and hydrophobic form (Fig. 4c,d). As highly cathodic potentials are applied, it is assumed that both the dendrites react rapidly with either H^+ or CO_2 to form Cu–H* or Cu–COOH* intermediates, respectively[36], and therefore selectivity is controlled by the mass transport of the two substrates. The wettable dendrite has a large liquid–electrode interface and therefore only the aqueous H^+/CO_2 are substrates (Fig. 4a). A higher proportion of Cu–H* groups is then expected, which promotes H_2 formation (Fig. 4b). Alternatively, the electrolyte is pushed away from the hydrophobic dendrite Cu surface to form an electrolyte–solid–gas triple-phase boundary at the electrode (Fig. 4c). CO_2 mass transport is then omnidirectional, whereas H^+ comes unilaterally from the bulk solution, which drastically increases the local CO_2 concentration. The surface concentration of Cu–COOH* and the subsequently formed Cu–CO* is then greatly increased over that of Cu–H*. This promotes C–C coupling and therefore the efficiency for C_2 products is increased (Fig. 4d). The reduction of CO without coupling is also possible, which explains the enhanced CH_4 production. Based on the presented CO reduction experiments, the selectivity for C_2 over CH_4 can be increased with a high solution pH, which corroborates recent reports that C_2 formation at a high overpotential is dependent on high concentrations of Cu–CO*, whereas CH_4 formation requires a rate-limiting electron–proton transfer to give a Cu–CHOH* intermediate[37].

Perhaps more interesting are the products from CO_2 reduction produced solely on the wettable dendrite, ethane and *n*-propanol, albeit in small quantities (below 5% FE). The lack of these products on the hydrophobic dendrite, as well as other highly efficient C_2-forming electrodes[19], suggests that hydrogen transfer is a rate-limiting step in their formation and therefore they require a high concentration of Cu–H*. This is supported by recent reports that show high efficiencies for CO_2 reduction to *n*-propanol with a relatively high H_2-evolution activity[38] and also reports of ethane formation on surfaces that generate large quantities of H_2 (ref. [39]).

The presented experiments led us to consider other reported catalysts for C_2 product formation, which traditionally have been Cu oxides[22]. Many explanations for their activity are available, but we hypothesize that the combination of nanostructured surfaces with hydrophobic Cu_2O (ref. [40]) forms similar voids that trap CO_2 to create an electrolyte–electrode–gas triple-phase boundary. Regions that are not in contact with electrolyte solution on these surfaces explain why oxides are still spectroscopically visible in operando[11], despite their expected removal at the cathodic potential[41]. It may also explain the low long-term stability of such surfaces, as removal of the oxides increases surface wettability. Further support for this concept is illustrated by stable C_2 product formation on gas-diffusion electrodes[19], whose hydrophobicity is not as susceptible to reduction and as such maintain their electrolyte–electrode–gas interfaces.

Conclusion

In summary, a hydrophobic coating of long-chain alkanethiols on dendritic Cu, with no further modification, led to a drastic increase in the CO_2 reduction selectivity. The difference is a result of a plastron effect; a gaseous layer trapped at the surface of the electrode that increases the local CO_2 concentration, which allows the Cu dendrite to match the high selectivity for C_2 products reported on Cu-loaded gas-diffusion electrodes[19]. In the present form, the electrode suffers from some drawbacks for its implementation in technological devices and future work will focus on promoting stable hydrophobicity on high-surface-area microporous electrodes to further increase activity.

We conclude that hydrophobicity, and the resultant gas-filled voids that it introduces, is a governing factor of CO_2 reduction selectivity on Cu and should be considered in the future design and understanding of electrocatalytic surfaces for both CO_2 and CO reduction.

Online content

Any methods, additional references, Nature Research reporting summaries, source data, statements of code and data availability and associated accession codes are available at https://doi.org/10.1038/s41563-019-0445-x.

Received: 7 January 2019; Accepted: 24 June 2019;
Published online: 5 August 2019

References

1. IPCC *Climate Change 2013: The Physical Science Basis* (eds Stocker, T. F. et al.) (Cambridge Univ. Press, 2013).
2. Raciti, D. & Wang, C. Recent advances in CO_2 reduction electrocatalysis on copper. *ACS Energy Lett.* **3**, 1545–1556 (2018).
3. Qiao, J., Liu, Y., Hong, F. & Zhang, J. A review of catalysts for the electroreduction of carbon dioxide to produce low-carbon fuels. *Chem. Soc. Rev.* **43**, 631–675 (2014).
4. Sander, R. Compilation of Henry's law constants, version 3.99. *Atmos. Chem. Phys. Discuss.* **14**, 29615–30521 (2014).
5. Hori, Y., Kikuchi, K. & Suzuki, S. Production of CO and CH_4 in electrochemical reduction of CO_2 at metal electrodes in aqueous hydrogencarbonate solution. *Chem. Lett.* **14**, 1695–1698 (1985).

6. Wang, J., Zhang, F., Kang, X. & Chen, S. Organic functionalization of metal catalysts: enhanced activity towards electroreduction of carbon dioxide. *Curr. Opin. Electrochem.* **13**, 40–46 (2019).
7. Zhou, Y. et al. Dopant-induced electron localization drives CO_2 reduction to C_2 hydrocarbons. *Nat. Chem.* **10**, 974–980 (2018).
8. Varela, A. S., Kroschel, M., Reier, T. & Strasser, P. Controlling the selectivity of CO_2 electroreduction on copper: the effect of the electrolyte concentration and the importance of the local pH. *Catal. Today* **260**, 8–13 (2016).
9. Piontek, S. et al. Bio-inspired design: bulk iron–nickel sulfide allows for efficient solvent-dependent CO_2 reduction. *Chem. Sci.* **10**, 1075–1081 (2019).
10. Li, Y. et al. Structure-sensitive CO_2 electroreduction to hydrocarbons on ultrathin 5-fold twinned copper nanowires. *Nano Lett.* **17**, 1312–1317 (2017).
11. De Luna, P. et al. Catalyst electro-redeposition controls morphology and oxidation state for selective carbon dioxide reduction. *Nat. Catal.* **1**, 103–110 (2018).
12. Tang, W. et al. The importance of surface morphology in controlling the selectivity of polycrystalline copper for CO_2 electroreduction. *Phys. Chem. Chem. Phys.* **14**, 76–81 (2012).
13. Jeon, H. S., Kunze, S., Scholten, F. & Roldan Cuenya, B. Prism-shaped Cu nanocatalysts for electrochemical CO_2 reduction to ethylene. *ACS Catal.* **8**, 531–535 (2018).
14. Reller, C. et al. Selective electroreduction of CO_2 toward ethylene on nano dendritic copper catalysts at high current density. *Adv. Energy Mater.* **7**, 1602114 (2017).
15. Dutta, A., Rahaman, M., Luedi, N. C., Mohos, M. & Broekmann, P. Morphology matters: tuning the product distribution of CO_2 electroreduction on oxide-derived Cu foam catalysts. *ACS Catal.* **6**, 3804–3814 (2016).
16. Huo, Y., Peng, X., Liu, X., Li, H. & Luo, J. High selectivity toward C_2H_4 production over Cu particles supported by butterfly-wing-derived carbon frameworks. *ACS Appl. Mater. Interfaces* **10**, 12618–12625 (2018).
17. Hoang, T. T. H. et al. Nanoporous copper–silver alloys by additive-controlled electrodeposition for the selective electroreduction of CO_2 to ethylene and ethanol. *J. Am. Chem. Soc.* **140**, 5791–5797 (2018).
18. Higgins, D., Hahn, C., Xiang, C., Jaramillo, T. F. & Weber, A. Z. Gas-diffusion electrodes for carbon dioxide reduction: a new paradigm. *ACS Energy Lett.* **4**, 317–324 (2019).
19. Dinh, C.-T. et al. CO_2 electroreduction to ethylene via hydroxide-mediated copper catalysis at an abrupt interface. *Science* **360**, 783–787 (2018).
20. Huan, T. N. et al. Low-cost high-efficiency system for solar-driven conversion of CO_2 to hydrocarbons. *Proc. Natl Acad. Sci. USA* **116**, 9735–9740 (2019).
21. Li, C. W. & Kanan, M. W. CO_2 reduction at low overpotential on Cu electrodes resulting from the reduction of thick Cu_2O films. *J. Am. Chem. Soc.* **134**, 7231–7234 (2012).
22. Mistry, H. et al. Highly selective plasma-activated copper catalysts for carbon dioxide reduction to ethylene. *Nat. Commun.* **7**, 12123 (2016).
23. Checco, A., Hofmann, T., DiMasi, E., Black, C. T. & Ocko, B. M. Morphology of air nanobubbles trapped at hydrophobic nanopatterned surfaces. *Nano Lett.* **10**, 1354–1358 (2010).
24. Melnichenko, Y. B. et al. Cavitation on deterministically nanostructured surfaces in contact with an aqueous phase: a small-angle neutron scattering study. *Langmuir* **30**, 9985–9990 (2014).
25. Zheng, D. et al. Salvinia-effect-inspired 'sticky' superhydrophobic surfaces by meniscus-confined electrodeposition. *Langmuir* **33**, 13640–13648 (2017).
26. Kopljar, D., Inan, A., Vindayer, P., Wagner, N. & Klemm, E. Electrochemical reduction of CO_2 to formate at high current density using gas diffusion electrodes. *J. Appl. Electrochem.* **44**, 1107–1116 (2014).
27. Neumann, D. & Woermann, D. Stability of the volume of air trapped on the abdomen of the water spider *Argyroneta aquatica*. *SpringerPlus* **2**, 694 (2013).
28. Hokmabad, B. V. & Ghaemi, S. Effect of flow and particle–plastron collision on the longevity of superhydrophobicity. *Sci. Rep.* **7**, 41448 (2017).
29. Huan, T. N. et al. Porous dendritic copper: an electrocatalyst for highly selective CO_2 reduction to formate in water/ionic liquid electrolyte. *Chem. Sci.* **8**, 742–747 (2017).
30. Huan, T. N. et al. A dendritic nanostructured copper oxide electrocatalyst for the oxygen evolution reaction. *Angew. Chem. Int. Ed.* **56**, 4792–4796 (2017).
31. Wang, Y., Im, J., Soares, J. W., Steeves, D. M. & Whitten, J. E. Thiol adsorption on and reduction of copper oxide particles and surfaces. *Langmuir* **32**, 3848–3857 (2016).
32. Dilimon, V. S., Denayer, J., Delhalle, J. & Mekhalif, Z. Electrochemical and spectroscopic study of the self-assembling mechanism of normal and chelating alkanethiols on copper. *Langmuir* **28**, 6857–6865 (2012).
33. Simpson, J. T., Hunter, S. R. & Aytug, T. Superhydrophobic materials and coatings: a review. *Rep. Prog. Phys.* **78**, 086501 (2015).
34. Schoenfisch, M. H. & Pemberton, J. E. Air stability of alkanethiol self-assembled monolayers on silver and gold surfaces. *J. Am. Chem. Soc.* **120**, 4502–4513 (1998).
35. Singh, M. R., Kwon, Y., Lum, Y., Ager, J. W. & Bell, A. T. Hydrolysis of electrolyte cations enhances the electrochemical reduction of CO_2 over Ag and Cu. *J. Am. Chem. Soc.* **138**, 13006–13012 (2016).
36. Kortlever, R., Shen, J., Schouten, K. J. P., Calle-Vallejo, F. & Koper, M. T. M. Catalysts and reaction pathways for the electrochemical reduction of carbon dioxide. *J. Phys. Chem. Lett.* **6**, 4073–4082 (2015).
37. Liu, X. et al. pH effects on the electrochemical reduction of CO_2 towards C_2 products on stepped copper. *Nat. Commun.* **10**, 32 (2019).
38. Rahaman, M., Dutta, A., Zanetti, A. & Broekmann, P. Electrochemical reduction of CO_2 into multicarbon alcohols on activated Cu mesh catalysts: an identical location (IL) study. *ACS Catal.* **7**, 7946–7956 (2017).
39. Chen, C. S., Wan, J. H. & Yeo, B. S. Electrochemical reduction of carbon dioxide to ethane using nanostructured Cu_2O-derived copper catalyst and palladium(II) chloride. *J. Phys. Chem. C* **119**, 26875–26882 (2015).
40. Zahiri, B., Sow, P. K., Kung, C. H. & Mérida, W. Active control over the wettability from superhydrophobic to superhydrophilic by electrochemically altering the oxidation state in a low voltage range. *Adv. Mater. Interfaces* **4**, 1700121 (2017).
41. Eilert, A. et al. Subsurface oxygen in oxide-derived copper electrocatalysts for carbon dioxide reduction. *J. Phys. Chem. Lett.* **8**, 285–290 (2017).
42. Seymour, R. S. & Hetz, S. K. The diving bell and the spider: the physical gill of *Argyroneta aquatica*. *J. Exp. Biol.* **214**, 2175–2181 (2011).

Acknowledgements

V.M. acknowledges financial support from CNRS-Cellule Energie and Fondation of Collège de France for the acquisition of the GC equipment. D.W. was supported by an Idex PSL grant (ANR-10-IDEX-001-02 PSL), the Fondation du Collège de France and the Marie Curie PRESTIGE Fellowship programme. S.L. was funded by the Corps des Ponts, des Eaux et des Forêts. X-ray diffraction measurements were carried out by G. Rousse at the Collège de France. SEM images were collected by D. Montero at the Institut des Matériaux de Paris and F. Pillier at the Laboratoire Interfaces et Systèmes Electrochimiques. BET measurements were carried by J. Blanchard at the Laboratoire de Réactivité de Surface at Sorbonne Université.

Author contributions

D.W., M.F. and V.M. conceived the research. D.W. and S.L. performed electrocatalysis and characterization. N.M. carried out TEM measurements. F.O., S.L. and D.W. carried out the infrared experiments. XPS was carried out by D.M. and P.M. All authors the analysed the data. D.W. wrote the manuscript. S.L., M.F. and V.M. added to the discussion and contributed to the preparation of the manuscript. M.F. and V.M. supervised the work.

Competing interests

Authors declare no competing interests.

Additional information

Supplementary information is available for this paper at https://doi.org/10.1038/s41563-019-0445-x.

Reprints and permissions information is available at www.nature.com/reprints.

Correspondence and requests for materials should be addressed to M.F. or V.M.

Publisher's note: Springer Nature remains neutral with regard to jurisdictional claims in published maps and institutional affiliations.

Methods

General. SEM images were performed on a SU-70 Hitachi FEGSEM fitted with an X-Max 50 mm^2 Oxford EDX spectrometer or a Hitachi S-4800 SEM. Powder X-ray diffraction was performed in a Bragg–Brentano geometry using a BRUKER D8 Advance diffractometer with Cu Kα radiation ($\lambda_{K\alpha_1}$ = 1.54056 Å, $\lambda_{K\alpha_2}$ = 1.54439 Å) and a Lynxeye XE detector. Contact angle measurements were made on a slow-motion video camera with 15 µl of H_2O. XPS spectra were performed using a Thermo ESCALAB 250 X-ray photoelectron spectrometer with a monochromatic Al-Kα X-ray source ($h\nu$ = 1,486.6 eV).

Preparation of Cu dendrites. Square Cu surfaces of 1 cm^2 surface area were prepared from a Cu plate (99.999%, 1 mm thickness, GoodFellow) that had its sides, back and backside electrical contact encased in epoxy resin (Loctite, Henkel). The surface was polished mechanically using an alumina micropolish on a polishing cloth (3 µm, Struers) followed by copious rinsing in water. Dendrite deposition was subsequently undertaken by applying −0.5 A cm^{-2} to the electrode for 120 s in a solution that contained 0.1 M $CuSO_4{\cdot}5H_2O$ (99.9%, Sigma Aldrich) in 1.5 M H_2SO_4 (Sigma Aldrich) followed by rinsing under a gentle stream of water and then acetone. The electrode was then dried under a stream of air.

Alkanethiol deposition. Application of 1-octadecanethiol (98%, Sigma Aldrich) was undertaken by first melting the waxy solid under vacuum at 60 °C. The electrode to be treated was then submerged into the liquid under Ar and left for 15 min at 60 °C. After this, the electrode was moved to a solution of ethyl acetate at 60 °C for 5 min to remove excess 1-octadecanethiol and then allowed to dry in ambient conditions.

Electrocatalytic analysis. Electrochemical analysis was carried out in an air-tight two compartment electrochemical cell separated by a Nafion membrane (N-115, Alfa Aesar) or bipolar membrane (Fumasep FBM, FuelCellStore). The counter electrode was a Pt wire (GoodFellow) and the reference a Ag/AgCl wire in 3 M KCl (PalmSens). The electrolyte was 0.1 M $CsHCO_3$ (99.9%, Sigma Aldrich), 1 M KOH (Sigma Aldrich) or 0.1 M KPi (0.054 M K_2HPO_4 and 0.046 M KH_2PO_4, Carl Roth), which was deaerated/saturated with CO_2/CO/Ar before each experiment by bubbling CO_2 (≥99.998%, Linde), CO (Linde) or Ar (Linde) for at least 10 min.

During electrolysis the electrodes were placed such that the gas bubble flow from the bottom of the vessel was at a 45° angle of incidence, as this ensured all the gas bubbles collided with the electrode surface. Gas was flowed through the cathode compartment of the cell using a mass flow controller (Bronkhorst) and the solution was stirred. The headspace was connected to a gas chromatograph (GC) (discussed below) and was typically sampled at 10 and 30 min. The liquid phase was analysed for products by ^{1}H NMR spectroscopy after 35 min (see below). FE was calculated based on the time before injection that was required to fill the GC sample injector loops (1 ml). This is summarized in equation (1):

$$\mathrm{FE}\ (\%) = \frac{n_{\mathrm{product}} \times n_{\mathrm{electrons}} \times F}{(Q_{t=0} - Q_{t=x})} \times 100 \qquad (1)$$

where $n_{product}$ is the product measured (mol), $n_{electrons}$ is the number of electrons to make said product from CO_2/H_2O or CO/H_2O, F is the Faraday constant (C mol^{-1}), $Q_{t=0}$ is the charge passed at the point of injection and $Q_{t=x}$ is the charge passed at x seconds before injection (C), x being the time required to fill the GC sample loop based on sample loop size and gas flow rate.

During the LSVs, the electrode was placed outside the CO_2 inlet, no stirring was applied and the CO_2 flow was decreased to 0.2 ml min^{-1}.

Potentials were converted to the RHE using the relationship: E (RHE) = E (Ag/AgCl) + 0.197 + (pH × 0.059). The ohmic-drop correction of the potentials applied during the CCE was undertaken manually using the resistance measured immediately after the electrolysis was completed. The reported potentials are those measured at the time point of GC analysis (typically 10 or 30 min). An ohmic-drop correction was not applied during CPEs, LSVs or cyclic voltammograms.

ECSA measurements. The ECSA was measured through the capacitance of the electrodes in a 0.1 M solution of $CsHCO_3$ (99.9%, Sigma Aldrich) saturated with CO_2. The capacitance was measured by analysis of the electrode cyclic voltammogram at −0.15 V versus the standard hydrogen electrode using equation (2):

$$\frac{i_a - i_c}{2} = Cv \qquad (2)$$

where C is the capacitance (F), i_a is the anodic current at −0.15 V versus the standard hydrogen electrode (A), i_c is the equivalent cathodic current (A) and v is the scan rate (V s^{-1}). The capacitance was found by plotting the left side of equation (2) against scan rate. The ECSA was then determined from the difference between the capacitance of the nanostructured surfaces relative to a flat 1 cm^2 Cu surface.

GC analysis. GC was carried out on an SRI instruments MG#5 GC with an Ar carrier gas. H_2 was quantified using a thermal conductivity detector and separated from other gases with a HaySepD precolumn attached to a 3 m molecular sieve column. All the carbon-based products were detected using a flame-ionization detector equipped with a methanizer and were separated using either a 3 m molecular sieve column (CO and CH_4) or a 5 m HaySepD column (C_2H_4 and C_2H_6). Calibration was performed using a custom mixture of each gas in CO_2.

^{1}H-NMR spectroscopy. ^{1}H-NMR spectroscopy was undertaken on a Bruker Avance III 300 MHz spectrometer at 300 K. A sample of the liquid phase electrolyte was taken and D_2O was added as a locking solvent, along with an aqueous terephthalic acid solution that served as a reference for quantification. A Pre-SAT180 water suppression method was carried out to remove the water peak from each spectrum[43].

BET. Surface areas were obtained from analysis of Kr-adsorption isotherms measured on a BelSorp Max set-up at 77 K. Prior to the measurement, samples were treated under vacuum at 130 °C for at least 7 h. Surface areas were estimated using the BET model (Kr cross-sectional area 0.210 nm^2). The BET sample was prepared by undertaking the described dendrite preparation procedure on a large Cu surface (3 × 3 cm^2) to grow enough dendrite for the measurement. Alkanethiol treatment of the large electrode was carried out by covering the dendrite in a powder of 1-octadecanethiol and inserting the resultant surface horizontally in a vacuum oven at 100 °C for 15 min. The electrode was subsequently removed and left in a bath of warm ethyl acetate at 60 °C for 5 min. Once dry, the dendritic Cu was carefully scraped off the underlying Cu support for analysis. The value derived from the BET measurement, reported in $m^2\,g^{-1}$, was converted to $cm^2\,cm^{-2}$ by multiplying it by the mass of deposited dendrite onto the 1 cm^2 flat Cu support (5 mg for the wettable dendrite and 4 mg for the hydrophobic dendrite).

TEM/STEM. TEM images and chemical maps were acquired with a Jeol 2100 F microscope operated at 200 kV and equipped with a UHR pole piece. X-ray energy-dispersive spectra were acquired in the STEM mode with the same microscope, equipped with a Jeol system for X-ray detection and cartography. EF-TEM images at zero loss and C-K edge data were acquired using a Gatan GIF 2991 spectrometer. Samples for TEM were prepared by shaking a lacey carbon TEM grid in a vial that contained a small amount of Cu dendrite powder.

ATR-FTIR spectroscopy. ATR-FTIR spectroscopy was carried on a 0.5 mm thick Si prism coated with 3–5 nm of Cu in a metal vacuum–evaporation apparatus. Alkanethiolation of the prism was undertaken as described above. ATR-FTIR spectroscopy was undertaken with the front of the prism exposed to a solution of 0.1 M $CsHCO_3$ under CO_2.

Data availability

Raw data used in preparation of this manuscript is available to download at https://doi.org/10.7910/DVN/DSPZHE.

References

43. Mo, H. & Raftery, D. Pre-SAT180, a simple and effective method for residual water suppression. *J. Magn. Reson.* **190**, 1–6 (2008).